Edinburgh Research Explorer

Planar Ni(II), Cu(II) and Co(II) tetraaza[14]annulenes: Structural, electronic and magnetic properties and application to field effect transistors

Planar Ni(II), Cu(II) and Co(II) tetraaza[14]annulenes: Structural, electronic and magnetic properties and application to field effect transistors**

Alexander M. Whyte,[1] Yoshiaki Shuku,[2] Gary S. Nichol,[1] Michio M. Matsushita,[2] Kunio Awaga[2] and Neil Robertson[1,]*

[1]EaStCHEM, School of Chemistry, Joseph Black Building, University of Edinburgh, West Mains Road, Edinburgh, EH9 3JJ, UK.

[2]Department of Chemistry, Graduate School of Science, and Research Center of Materials Science, Nagoya University, Chikusa-ku, Japan.

[*]Corresponding author; e-mail: neil.robertson@ed.ac.uk, fax: +44 (0)131 650 4743, tel: +44 (0)131 650 475

Supporting information:
[†] Electronic supplementary information (ESI) available. CCDC 882247–882250. For ESI and crystallographic data in CIF or other electronic format see http://dx.doi.org/10.1039/C2JM33079B

Abstract

A series of planar Ni(II), Cu(II) and Co(II) tetraaza[14]annulenes has been prepared and studied optically, electrochemically and magnetically. Thin films of each of these complexes have been prepared by vacuum deposition to evaluate the field-effect transistor (FET) performance as well as the morphology and crystallinity of the film formed. The electrochemistry and UV/Vis absorption studies indicate the materials are redox active and highly coloured, with molar extinction coefficients as large as 80,000 $M^{-1}cm^{-1}$ in the visible region. The paramagnetic complexes display weak antiferromagnetic interactions, fit to the Bonner-Fisher chain model. Each of the materials formed polycrystalline films when vacuum deposited and showed field-effect transistor behaviour, with charge carrier mobilities in the range of 10^{-5} to 10^{-9} cm^2 V^{-1} s^{-1}. SEM imaging of the substrates indicates that the central metal ion, and its sublimation temperature, has a crucial role in defining the morphology of the resulting film.

Introduction

Porphyrins and phthalocyanines represent some of the most promising candidates for a range of applications due to their fascinating optical and electronic properties.[1] These planar, π-conjugated macrocycles commonly find widespread use as the semiconducting layer in field effect transistors,[2-4] organic light emitting diodes[5] and as the light harvesting component in solar cells.[6, 7] An attractive feature is the ability to functionalise the periphery and/or incorporate a wide range of metal ions into the central cavity of these macrocycles, in order to tune their physical, optical and electronic properties. In addition to its electronic effect, it has previously been demonstrated that the size of the central metal ion can play a key role in the charge carrier mobility, by dictating the intermolecular distance in the crystal lattice,[8] with the smaller metal facilitating better overlap of the ligand based frontier orbitals.

Although porphyrins have been utilised less in FETs compared with other organic electronic devices,[9] these molecules typically demonstrate p-type conductivity with respectable mobilities in the range of 10^{-6} to 10^{-1} $cm^2V^{-1}s^{-1}$.[4] Phthalocyanines on the other hand, have slightly higher reported mobilities in the range 10^{-3} to 1.0 $cm^2V^{-1}s^{-1}$ depending on the central metal and the device specifications.[10, 11] An interesting feature of phthalocyanine chemistry is that their semiconducting behaviour can be switched from p-type to n-type, going from the unsubstituted compound to the hexadecafluorinated analogue.[12, 13] Along with their attractive qualities such as planarity, high number of π-electrons and suitable crystal packing, the high thermal and chemical stability of these macrocycles is of importance in FET applications as this allows high purity films to be easily grown by vacuum sublimation techniques.[14]

A well known, but less studied, porphyrin analogue is the class of dibenzotetraaza[14]annulenes.[15] These tetradentate ligands commonly bind metal ions in the dianionic form but complexes have also been reported

from the neutral ligand.[16] The geometry of the macrocycle can vary depending on the substituents on the 1,3-propanediiminato linkage and the size of the metal ion in the central cavity.[17] In the absence of any substituents on the 1- or 3-positions of the propanediiminato moiety, then the free ligand is usually planar but the introduction of methyl groups into these positions will disrupt this planarity, through steric interactions with the benzene ring, and the ligand will adopt a buckled or saddle shaped conformation. Thus substituents on the 1- or 3-positions of the propanediiminato linkage will result in marked changes in the solid state crystal packing, which has important implications for conducting applications.
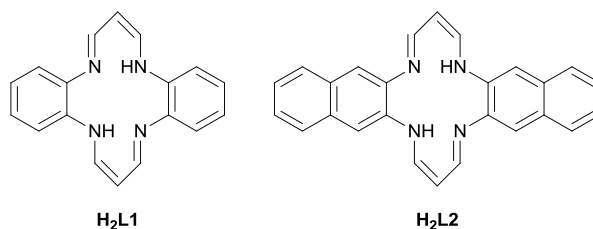
Figure 1. Structures of dibenzo[14]tetraazaannulene (H$_2$L1) and dinaptho[14]teraazaannulene (H$_2$L2).

In this work we have examined the electronic, magnetic, optical and charge transport properties of a series of metal complexes using tetraazaannulene macrocyclic ligands (Figure 1). This class of macrocycle has been previously shown to exhibit conductive behaviour when doped with iodine,[18] but despite this, the thin film charge transport properties have until now been unexplored.

Results and Discussion

1. **Crystallography**

The single crystal structure of Ni(L1) and the unit cell dimensions of Co(L1) have previously been reported[19] and were shown to be isomorphous. Single crystals of Ni(L1) grown in our lab match the unit cell dimensions previously reported. However, we have also grown crystals of Co(L1) and found the structure to be orthorhombic rather than monoclinic as was previously reported along with the unit cell dimensions.[19] Herein we also report the single crystal structure of the analogous Cu(L1) complex and of Ni(L2). In addition, a Co(III) complex, Co(L1)Cl, has been isolated by recrystallising Co(L1) from DCM and toluene (Table S1).

Unlike Ni(L1), the crystal structure of Co(L1) contains one molecule in its asymmetric unit. The molecules are packed in a herringbone motif with short, equidistant 1-D interplanar distances of 3.240 Å. The π-stacking is slipped with the propanediimine linkages overlapping effectively with a short contact of 3.29(2) Å, similar to what is observed in Ni(L1) and Cu(L1) (*vide infra*). The geometry around the Co(II) centre is square planar, as expected, with varying Co-N bond lengths of 1.896(11), 1.886(10), 1.836(11) and 1.870(10) Å. The N-Co-

N bite angles are 84.7(7) and 87.0(6)°. The short contact between the Co(II) centre and the closest C atom on the adjacent molecules is 3.45(1) Å indicating that a possible axial Co-C interaction could be present.
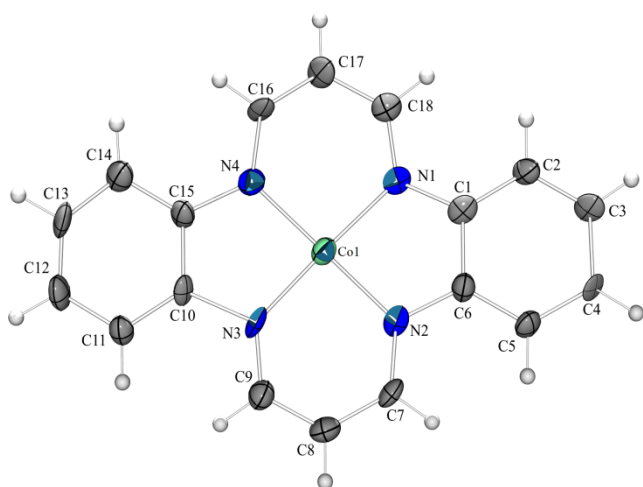
← *Figure 2.* Structure of Co(L1). Displacement ellipsoids are at the 50% probability level.

Unsurprisingly, the crystal structure of Cu(L1) is isomorphous to Ni(L1). The asymmetric unit contains two crystallographically-independent Cu(L1) molecules, with each ligand coordinating Cu(II) in a square planar manner. With regard to the environment around the metal centre, the first Cu(L1) molecule shows Cu-N bonds of 1.926(2) and 1.927(2) Å, with the second molecule displaying Cu-N lengths of 1.927(2) and 1.928(1). These bonds are slightly longer than the Ni-N lengths of 1.869(2) and 1.872(2) Å, and 1.868(2) and 1.871(2) Å reported for Ni(L1).[19] The N-Cu-N bite angles within the diaminobenzene fragment of 84.50(7)° and 84.53(7)° are similar to the 85.25(8)° and 85.16(9)° reported in the case of Ni(L1). Similar to Co(L1), the material crystallises in a herringbone fashion with short 1-D interplanar distances (3.238 Å) (Figure 3. The planar, aromatic nature of the complexes combined with the short interplanar distances makes these molecules suitable candidates for study as conducting materials. The molecules are π-stacked in a slipped fashion with the propanediimine linkages overlapping, but with very little overlap of the aromatic rings (Figure 4). The short contact between the Cu(II) centre and the closest C atom on the adjacent molecules at 3.468(2) Å is similar to that observed in Co(L1).
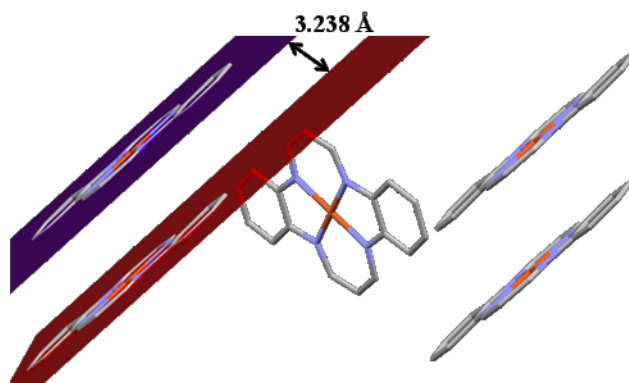
Figure 3. → Crystal packing of Cu(L1) showing short interplanar distances.
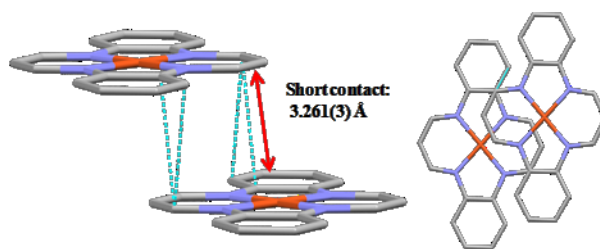
Figure 4. Molecular overlap of Cu(L1) as it stacks along the b-axis.

From the single crystal structure of Ni(L2) (Figure 5) it can be seen that, surprisingly, the increased π-conjugation of the naphthalene ring has resulted in a non-planar structure. This non-planarity has resulted in a larger face-to-face π-stacking distance (~6 Å) but the edge to face π-stacking distance is much shorter (~2.5 Å) (Figure 6). The non-planar structure may be a result of crystal packing forces, which have forced the molecule to adopt a twisted geometry to minimise repulsive interactions between naphthalene rings. In contrast to Cu(L1) and Ni(L1), the asymmetric unit of Ni(L2) contains only one molecule. The Ni-N distances of 1.866(2) and 1.865(2), as well the N-Ni-N bite angle of 84.98(9)° indicate that the coordination environment around the metal centre is almost identical to what was observed with Ni(L1).
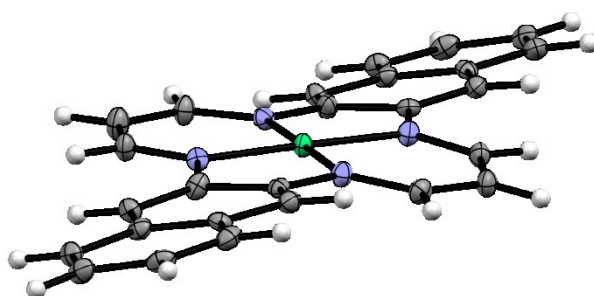
Figure 5. The crystal structure obtained for Ni(L2).
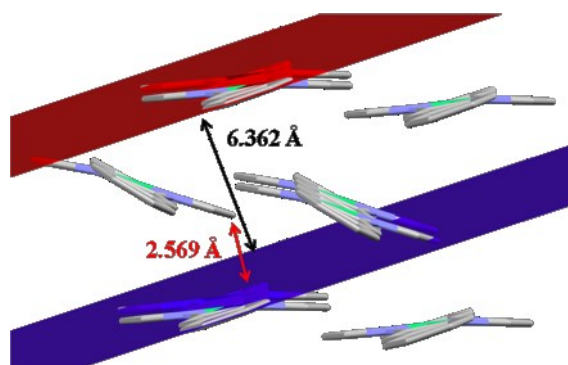
Figure 6. Crystal packing of Ni(L2).

The unit cell of Co(L1)Cl is shown in the supplementary information (Figure S1). The coordination geometry around the Co(III) centre is square based pyramidal with the chloride ion bound in the axial position. In contrast to Cu(L1) and Ni(L1), it appears that the metal centre in Co(L1) is susceptible to oxidation when to left to crystallise in dichloromethane under an air environment over a period of a week. However, when in the solid, powder form Co(L1) is air stable indefinitely. Solvent of crystallisation is also present in the unit cell; in this case toluene is present in a 1:1 ratio with the complex, although the solvent has a high degree of disorder. Since the complexes will be thermally evaporated onto substrates in the absence of solvent, the solid state packing of Co(L1)Cl is not relevant in rationalising the FET performance.

2. Electrochemistry

Despite the poor solubility of these planar molecules, cyclic voltammetry (CV) measurements on L1 have previously been reported,[20] with the macrocycle displaying several electrochemically accessible redox processes at -1.77, 0.75 and 1.06 V (vs. saturated calomel reference electrode). However, owing to the poor solubility of the metallated macrocycles we found differential pulse voltammetry (DPV) to be a more useful technique in the study of these materials due to its enhanced sensitivity. The effect of a metal centre on these potentials is shown in Table 1. The differential pulse and cyclic voltammograms are given in the supplementary information (Figure S6-S11,S13-S16).

Table 1. Redox potentials as measured by differential pulse from -2 to 1.8 V.

Sample	E_{pc} (V)	E_{pa} (V)
Co(L1)	-1.07, -1.41, -1.62, -1.89	0.24, 0.79, 1.30, 1.51, 1.73
Cu(L1)	-1.49	0.52, 1.08, 1.41
Ni(L1)	-1.68	0.66, 1.38
Ni(L2)	-1.67	0.46, 0.99, 1.72

The cyclic voltammetry analysis of these complexes is hampered by the poor solubility of the macrocyclic complexes, but in the case of Ni(L1), which appears to be the most soluble, some interesting behaviour was observed. When the potential was scanned from 0 to 2 V, 2 to –2 V and then back to 0 V, two oxidations were observed at positive potential, 0.72 and 1.40 V, and one reduction at negative potential, -1.77 V (Figure S11). On repeating this scan a further four times, the reduction process disappears completely and the first oxidation at 0.66 V grows in intensity. The second oxidation peak changes in shape after the second scan and appears at a less positive potential; at 1.20 V by the fifth scan. This behaviour is indicative of a deposited film forming on the working electrode and this was seen to be the case when the electrode was removed from solution (Figure S12). In fact, the electrochemical polymerisation of similar compounds has already been reported.[21, 22] Macrocycles of this type have previously been shown to first dimerise through the meso- position of the propanediimine linkage,[23] before then undergoing further polymerisation under an applied potential. On further studying Ni(L1) in the range –2 to 1 V we found that the oxidation and reduction potentials are largely unchanged, except that the current associated with the reductive process is decreasing (Figure S13). The peak potentials still occur in the same position, indicating that when scanning to this less positive potential the sample is not polymerising, and that, although not electrochemically reversible, there is potentially some chemical reversibility associated with the oxidation. The solubility of the other three complexes is lower than that of Ni(L1), making meaningful analysis by CV challenging; peaks appear broad with little definition and small peak current. Therefore, assessment of the reversibility of their redox processes becomes difficult.

In comparison to the other the complexes, Co(L1) displays many more redox processes when studied using differential pulse voltammetry. This could be partly due to the facile nature of the Co(II) to Co(III) oxidation but the number of additional processes could indicate the complex is decomposing or structurally changing. As shown earlier (Figure S1) it is possible for Co(L1) to be oxidised to Co(L1)Cl in the presence of DCM, thus it is plausible that additional redox processes could be the result of this species also existing in solution.

In summary, each of the materials displays at least two oxidations and one reduction, and these processes appear to be electrochemically and mostly chemically irreversible. The electrochemistry however indicates two important things, Firstly, in each of the complexes, with the exception of Co(L1), the frontier orbitals are predominantly ligand based, shown by the similarity in redox processes between the Cu and Ni examples. Secondly, due to the energies of the frontier orbitals the complexes are more suitable as electron donating materials than electron acceptors in FET devices.

3. Magnetic Measurements

Susceptibility measurements were carried out on Cu(L1) and Co(L1) over the temperature range 1.8 – 300 K. The data were fit to the Curie-Weiss law. For Cu(L1), the Curie constant obtained (Figure S18) of 0.392 cm^3 K mol^{-1} is in good agreement with that expected for an S=1/2 paramagnet. A small, negative Weiss constant

of -0.496(6) K was also obtained, suggesting weak antiferromagnetic exchange interactions. Analysis of the crystal packing indicates that the Cu(L1) molecules stack as 1D, linear chains, therefore data were fit to the modified Bonner-Fischer model, appropriate for linear chains of Heisenberg spins (H = -JΣS$_i$S$_{i+1}$),[24] over the range 1.8-300 K (Figure 7). From the experimental fitting, the following parameters were obtained; g of 2.04(1) and J of -0.4(1) cm^{-1}. The g value deviates from the free electron value indicating that, as we expect, the unpaired electron is significantly metal based, and the small J value indicates the intermolecular magnetic interaction is weak, consistent with the Curie-Weiss fit.
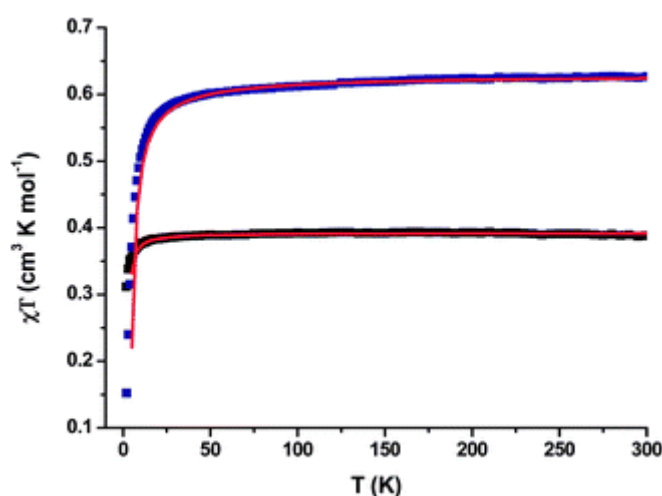
Figure 7. χT vs. T of Cu(L1) in black (lower curve), and Co(L1) in blue (upper curve). The curves of Cu(L1) and Co(L1) have been corrected for temperature independent paramagnetic (TIP) contributions of 3.56 x10^{-4} cm^3 mol^{-1} and 2.61 x10^{-4} cm^3 mol^{-1}, respectively. The solid red lines are the fits to the Bonner-Fisher model for a linear chain of Heisenberg S = ½ centres.

In contrast to the Cu(II) analogue, the Curie-Weiss plot of Co(L1) (Figure S17) gives the Curie constant as 0.639(2) cm^3 K mol^{-1} and the Weiss constant as -3.2(1) K, suggesting the antiferromagnetic exchange interaction is greater than in Cu(L1). Consistent with this, fit to the Bonner-Fisher model also indicates much stronger magnetic coupling with a J value of -2.4(1) cm^{-1} and a g-value of 2.59, within the range expected for Co(II) (Figure 7). For an S = ½ ion with g = 2.59, a Curie constant of 0.63 cm^{3}Kmol^{-1} is predicted, consistent with the Curie-Weiss fit. From computational calculations in the gas phase, it has been predicted that the unpaired electron of Co(L1) resides predominantly in the dxy orbital, whereas with Cu(L1) the unpaired electron is based in the dx^2-y^2 orbital. It is perhaps surprising that the magnetic exchange interactions differ so greatly, given that in both cases, the SOMO lies in the molecular plane and therefore it could reasonably be expected that similar superexchange interactions should be prevalent. A stronger interaction between molecules in the Co(II) derivative, which may have some bearing on the magnetic exchange, was noted

experimentally during sublimation; much higher temperatures were required to volatilise Co(L1) compared to Cu(L1). Interestingly, in related compounds such as Co(II) phthalocyanine, the unpaired electron has been found to be based predominantly in the dz^2 orbital.[25] If the unpaired electron in our system were based in the dz^2 orbital then axial Co-π interactions would help to rationalise the behaviour we observe.

4. Electronic Structure Calculations

Calculations have been used to understand the nature of the frontier orbitals as well as assign the electronic transitions witnessed by absorption spectroscopy. In the case of the dibenzotetraazaannulene (L1) complexes, molecular structures obtained from geometry optimisations at the B3LYP/6-31G(d,p) level of theory were in good agreement with the structures obtained by crystallisation in terms of bond lengths, bond angles and overall planarity of the molecule. With regard to Ni(L1), the electronic structure of the frontier orbitals is depicted in the supplementary information (Table S3), indicating the HOMO and LUMO are ligand based π-orbitals. A similar theme is witnessed with Co(L1) and Cu(L1); in both cases the HOMO and LUMO are ligand based π-orbitals, with the unpaired electron residing in a SOMO lower in energy than the ligand based HOMO (Table S4 and S5). In the case of Cu(L1) it is quite clear from the orbital energies and the spin density image that the unpaired electron is based in the dx^2-y^2 orbital (Figure S21), which is the α-HOMO-1 orbital. An additional study of the electronic structure of Cu(L1) at the UB3LYP/TZVP level (Figure S22) indicates a similar ordering of the filled molecular orbitals, with the energies of the frontier orbitals in reasonable agreement. For Co(L1), the unpaired electron is based in the α-HOMO-1 and the spin density (Figure S20) is metal centred, lying out of the plane of the molecule and in keeping with the greater magnetic exchange observed for Co(L1) compared with Cu(L1).

In the case of the dinapthotetraazaannulene (L2) complex, the optimised geometry varies significantly from that obtained by crystallisation (Figure S19) in terms of planarity, but both conformations, crystallised and geometry optimised, still show excellent agreement when comparing bond lengths and angles. There also appears to be more metal character to the frontier orbitals compared with the L1 complexes (Table S3), with both the HOMO and LUMO delocalised across the metal and ligand.

From TD-DFT calculations using the same basis set, the calculated absorption spectrum of Ni(L1) shows good agreement with the experimental data, with regard to peak absorption position and molar absorptivity (Figure 8). From calculations, the peak absorbance measured at 425 nm (calculated 387 nm) has been assigned to an excitation from the HOMO to LUMO+1 energy level. The peak at 290 nm in the TD-DFT generated spectrum has been assigned as HOMO-6 to LUMO. An assignment of the low energy, high intensity peaks is shown below (Table 2) with a complete assignment of transitions for each of the complexes given in Table S6.
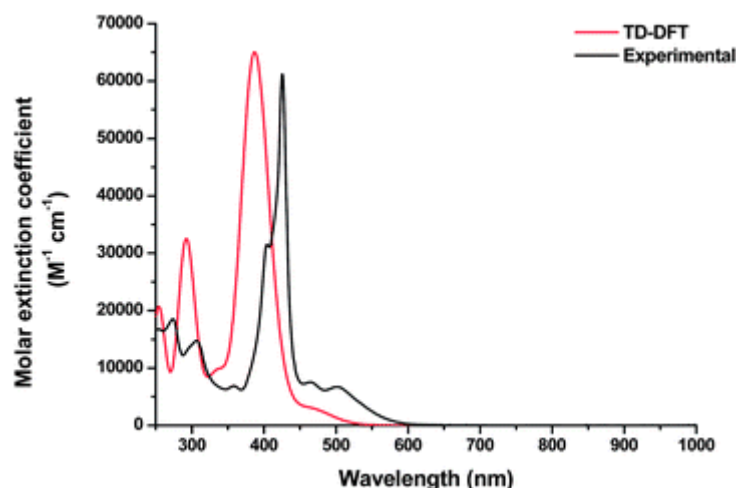
Figure 8. TD-DFT generated spectra (red) overlaid with the experimental plot (black) of Ni(L1).

The TD-DFT generated spectrum of Cu(L1) is also in general agreement with the experimental data. The TD-DFT generated spectrum of Co(L1) displays the absorption maxima in the same region as that observed experimentally but the magnitude of the molar extinction coefficient is not well estimated (Figure S24). The experimental value is approximately half the predicted value. It is possible this indicates difficulty in dissolving the complex, leading to an underestimation of the experimental value of the absorption coefficient. This may also apply to Ni(L2) below.

As expected, the absorption spectrum of Ni(L2) displays a bathochromic shift when compared to Ni(L1), as a result of the increased conjugation from the naphthalene moiety. Despite the experimental and calculated spectra closely resembling each other in terms of peak position, the molar extinction coefficient has also been calculated to be larger than the experimental value in the case of Ni(L2). The materials all display a similar HOMO-LUMO gap of around 3 eV but since none of these complexes show a direct HOMO-LUMO transition from TD-DFT, it is not possible to estimate the magnitude of this splitting, both in solution and solid state, by absorption spectroscopy. Therefore we should exercise caution when trying to directly compare HOMO-LUMO gaps measured by electrochemical methods with those estimated from absorption spectroscopy.

Table 2. TD-DFT assignment of electronic absorption spectra. Only λ max values are shown. H and L correspond to HOMO and LUMO; A and B correspond to alpha and beta orbitals.

Sample	Measured absorption (nm)	Calculated absorption (nm)	Oscillator strength	Major contribution
Co(L1)	392	345	1.0341	H-1(A)-> L(A) (11%), H(A)-> L+1(A) 13%), H-3(B)->L(B) (51%)
Cu(L1)	406	363	1.3016	H-2(A)-> L(A) (29%), H(A)-> L+1(A) (12%), H-1(B)-> L(B) (22%), H(B)->L+1(B) (15%)
Ni(L1)	425	387	0.8806	HOMO->L+1 (72%)
Ni(L2)	452	419	1.5829	H-1->LUMO (67%), HOMO->L+1 (10%)

5. Thin film XRD

The thin film diffraction patterns from each of the dibenzotetraazaannulene metal (II) complexes display a single reflection indicating the thin films are highly ordered. In each case the reflection at approximately 9° (2θ) is attributed to the (200) plane (Figure S28), by comparison with the single crystal data. The XRD pattern of Ni(L1) is shown below (Figure **9**) with the isomorphous Co(II) and Cu(II) analogues shown in the ESI (Figure S26 and S27). The thin film diffraction pattern for all of these complexes on Si (100) indicates the molecules are stacking edge-on onto the substrate. Assuming that the surface of the Si substrate has oxidised in air over time, we should expect a similar molecular orientation in our FETs, where the gate dielectric is SiO_2. This molecular alignment on the substrate is highly desirable in FET devices, as it means that the 1-D stacking axis is parallel to the substrate facilitating charge transport between the source and drain electrodes.
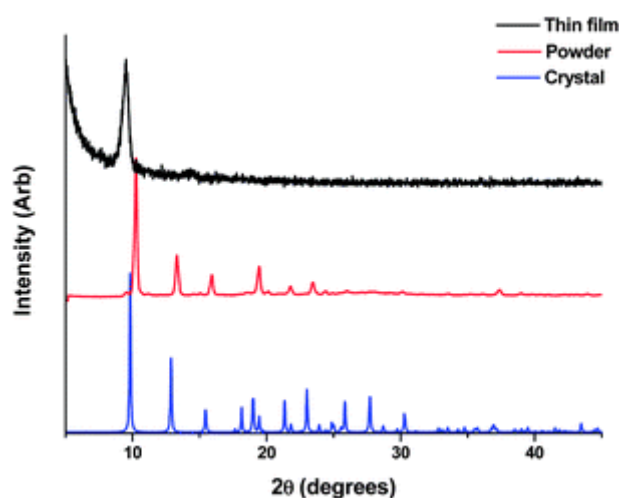

Figure 9. Thin film diffraction pattern of Ni(L1) in black, overlaid with the powder pattern (red) and the predicted powder pattern from the single crystal data (blue).

Although the diffraction pattern of Ni(L2) appears to be ordered with the molecules stacked in a particular orientation, the film is not as crystalline as the films produced by the dibenzo- analogues, judging from the peak width and intensity (Figure 10). Indexing the thin film pattern is not straightforward as both the powder and single crystal patterns exhibit two reflections, corresponding to different planes, very close to one another – the reflection from the thin film sample could correspond to either of these planes. From the single crystal structure, the peak at 8.23° (2θ) corresponds to a reflection from the (110) plane and the peak at 8.73° (2θ) is from the (200) plane (Figure S29). Therefore, elucidating the orientation of the molecules on the substrate is not possible. Note also, comparison between the powder diffraction and the predicted powder pattern from the single-crystal structure of this complex suggests differences in the phase (or phases) present in the powder compared with the single crystal.
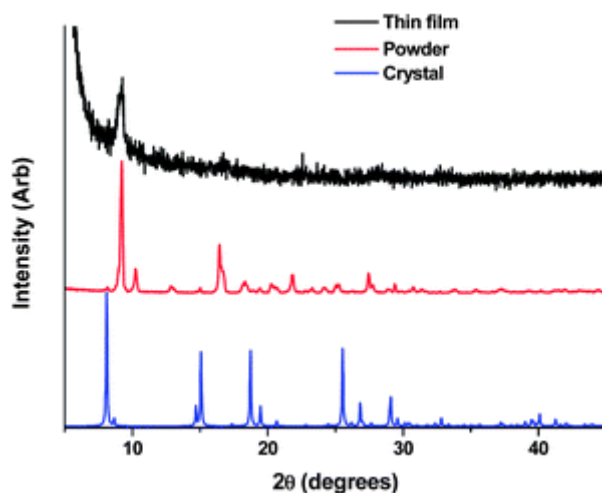
Figure 10. Thin film diffraction pattern of Ni(L2) in black, overlaid with the powder pattern (red) and the predicted powder pattern from the single crystal data (blue).

6. Thin film absorption spectroscopy

Films deposited onto quartz substrates were studied by absorption spectroscopy and contrasted with solution measurements to see if any change is witnessed between the spectra obtained from an isolated molecule in solution and the spectra obtained from a solid sample. The solution and film spectra are similar and as expected, each of the thin film spectra displays a significant broadening compared to solution measurements (Figures S21-S23). The lack of any large change indicates intermolecular interactions are relatively weak consistent with a material where weak non covalent interactions are prevalent. Interestingly, in the case of Ni(L2) the peak absorbance has red shifted slightly (Figure 11), which could indicate the formation of a band like structure resulting from the intermolecular interactions in the thin film. The dibenzotetraaazaannulenes display no such red shifting of the maximum, which may indicate the naphthalene ring is increasing the

strength of intermolecular interaction in the solid state. Since these films appear to be poorly crystalline from the thin film XRD results, the bathochromic shift could also be due to the material forming amorphous aggregates in the solid state.
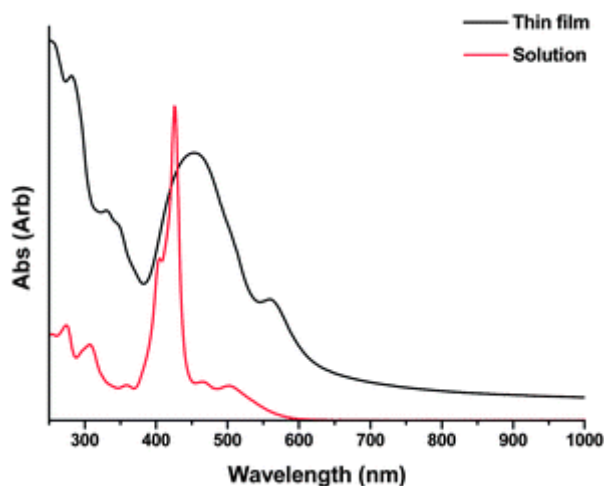
Figure 11. Thin film absorption of Ni(L2) with solution spectrum overlaid.

7. SEM

The micrographs were taken on FET substrates with an electrode width of 2 μm and gap of 8 μm. The image of Ni(L1) (Figure **12**) indicates a polycrystalline thin film with many grain boundaries between the electrodes; individual crystallites themselves are very small, less than 1 μm. FET measurements were also carried out on substrates with an electrode gap and width of 2 μm so the crystallites themselves are not large enough to bridge the gap between the source and drain.
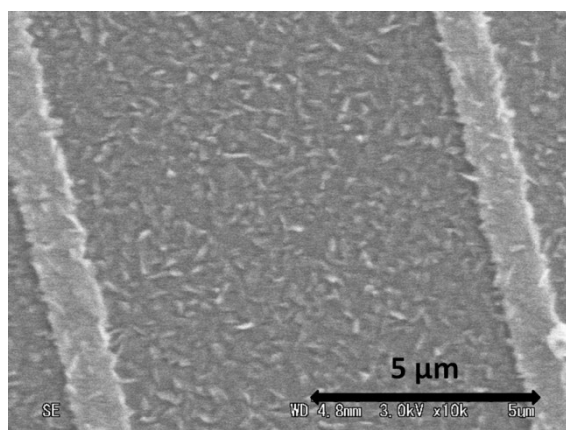
Figure 12. SEM image of Ni(L1) on a SiO$_2$ substrate with Au electrodes.

Similar to Ni(L1), the thin films of the Co(II) analogue appear to display a polycrystalline morphology consisting of very small crystallites (Figure 13). However, this image shows dark islands in amongst the film, possibly indicating the substrate coverage is not homogeneous. Such a discontinuous film is not observed in the micrographs of the other films that were imaged.
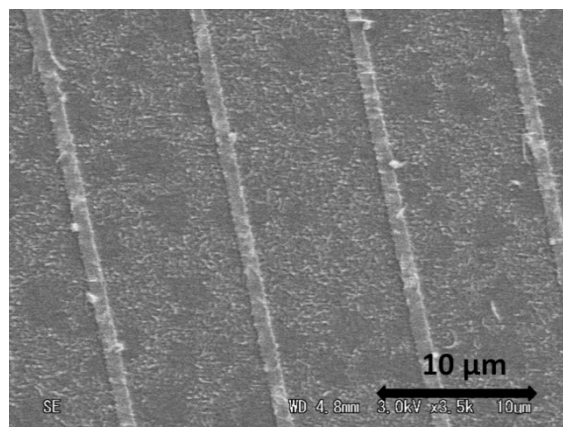
Figure 13. SEM image of Co(L1) on a SiO_2 substrate with Au electrodes.

Despite several attempts, it was not possible to acquire a satisfactory SEM image of Cu(L1) where the surface morphology could be resolved. The micrograph of Ni(L2) (Figure S33) shows a crystalline film but again the crystallites are very small, presenting many grain boundaries to the movement of charge carriers.

8. FET Measurements

As expected from the electrochemistry results, each of the four samples is an electron donor and, in keeping with this, we observed hole transport behaviour in a device with gold source and drain electrodes. The hole mobilities have been calculated from the transfer characteristics using Equation 1.

Equation 1 $\quad \mu = \frac{\partial I_{DS}}{\partial V_{GS}} \left(\frac{L}{C_i \, W \, V_{DS}} \right)$

The on/off ratios extracted from the transfer characteristics have been taken where the "on" current is the I_D value at V_G= -60 V and the "off" current is I_D at V_G= 0 V. The threshold voltage, at which the FET is effectively switched on, has been estimated by fitting a straight line to the linear regime in the transfer curve and extrapolating the point at which the x-axis is intercepted.

Ni(L1) and Cu(L1) display similar FET performance with regard to charge carrier mobility. Both values are of the same order of magnitude, but there is a marked difference in the on/off ratio (Table 3). In comparison, the mobilities of Co(L1) and Ni(L2) are much lower. The poor performance of Ni(L2) can be explained by the weak face to face π-stacking in the solid state, with the resulting large interplanar distance affecting the charge carrier mobility. The thin films produced from this material appear to be poorly crystalline compared with the dibenzo (L1) analogues, which could also explain the low mobility as crystal boundaries or structural inhomogeneity can result in traps to the movement of charge carriers.[26, 27] The large difference in the mobility and on/off ratio of Co(L1) compared with its isostructural Cu(II) and Ni(II) analogues may simply be due to incomplete surface coverage between the source and drain electrodes of the FET (Figure 13), which may have resulted from the different depositions temperatures required to volatilise Co(L1). However, each of the complexes displays a well defined gate effect judging from the output characteristics (Figure 14, S34, S38 and S40).
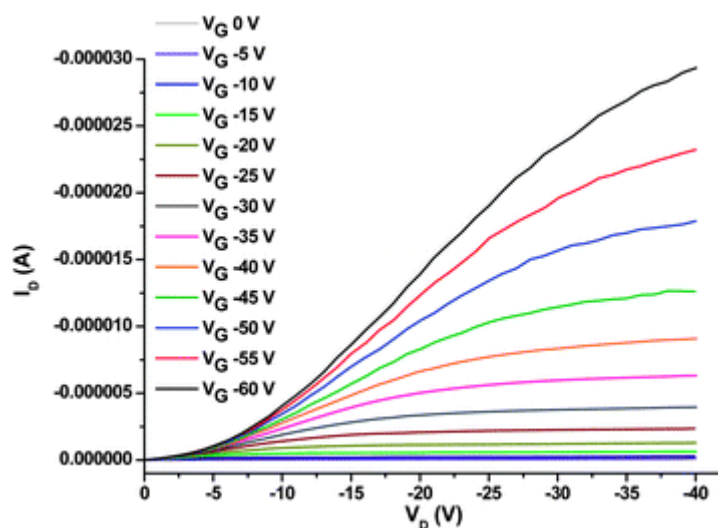
Figure 14. Output characteristics of Cu(L1) on 2x2 μm substrates

Table 3. FET results from measurements carried out on devices with an electrode gap and width of 2 μm.

Sample	On/off ratio	Threshold voltage (V)	Mobility (cm² V⁻¹ s⁻¹)
Co(L1)	96	-12	1.72×10^{-8}
Cu(L1)	3500	-26	1.55×10^{-5}
Ni(L1)	21,000	-19	2.57×10^{-5}
Ni(L2)	560	-14	4.79×10^{-9}

Magnetoresistance measurements were carried out on the Cu(L1) sample at cryogenic temperatures but the conductivity of Co(L1) was too low to study at low temperatures. A constant gate voltage, along with a source-drain voltage, was applied to the Cu(L1) sample as the source-drain current was measured. In the absence of an applied gate potential the material fails to conduct a measurable source-drain current. The IV characteristics of Cu(L1) were studied at various temperatures down to 4.35 K under a magnetic field swept between 5 T and -5T. However, no significant magnetoresistance was witnessed. At 4.35 K a small positive magnetoresistance (Figure S37) was observed but this was attributed to Lorentz forces from the magnetic field scattering the charge carriers flowing perpendicular to the field, as opposed to an intrinsic material property.

Conclusions

We have prepared a series of planar Ni, Cu and Co tetraaza[14]annulene macrocyles and have carried out the first assessment of these porphyrin analogues in thin-film devices. All the complexes exhibit p-type semiconductivity with a gate effect in an FET configuration. Despite forming highly ordered thin films, the hole mobilities are low. This can be rationalised by examination of the SEM images, which indicate polycrystalline films with many grain boundaries. Accordingly, improvement of the film crystallinity is likely to lead to much enhanced FET performance and this provides an area for future study using modified tetraazaannulene ligands. Variation of the central metal has a marked impact on the resulting FET properties. The key influence of the metal is in influencing the sublimation temperature and the resulting film morphology. The different compounds necessitate slightly different deposition conditions due to their different solid state interactions, leading to different degrees of crystallinity in the films, even for isomorphous materials. Due to the dominant effect of the film morphology, it is difficult to directly compare the role of the central metal between analogous complexes in terms of its electronic influence. Such a study would require comparison of single crystal FET results or films of consistent morphology. Given however, the consistent observation of gate-modulated transport across this series despite the non-ideal film characteristics, these complexes provide an interesting alternative to porphyrins in the study of metal complexes for FETs, with potential also in other electronic and optical devices. Following these initial promising results, their properties may be further optimised through ligand modification and associated optimisation of thin-film morphology and work in this direction is underway.

Experimental

All chemicals were purchased from Sigma Aldrich and used without further purification with the exception of o-phenylenediamine, which was recrystallised from DCM prior to use. The complexes were synthesised from o-phenylenediamine, 1,1,3,3-tetramethoxypropane and the corresponding metal(II) acetate salt, using an

approach adapted from the literature.[28] The resulting complexes were purified by vacuum sublimation. Single crystals of each of the complexes were grown by vacuum sublimation, with the exception of Co(L1).Cl, which was grown from DCM/toluene by slow evaporation.

Ni(L1). ^{1}H NMR (CDCl$_3$): 5.44 (t, 2H), 6.90 (m, 4H), 7.35 (m, 4H), 7.71 (d, 4H). MS (EI): m/z (%) = 344.1 (100.00%) [M$^+$]. Calculated for C$_{18}$H$_{14}$NiN$_4$, C 62.66, H 4.09, N 16.24; found C 62.55, H 3.98, N 16.13.

Cu(L1). MS (EI): m/z (%) = 349.0 (100.00%) [M$^+$]. Calculated for C$_{18}$H$_{14}$CuN$_4$, C 61.79, H 4.03, N 16.01; found C 61.63, H 3.91, N 15.92.

Co(L1). MS (EI): m/z (%) = 345.0 (100.00%) [M$^+$]. Calculated for C$_{18}$H$_{14}$CoN$_4$, C 62.62, H 4.09, N 16.23; found C 62.69, H 3.97, N 16.18.

Ni(L2). MS (EI): m/z (%) = 444.1 (100.00%) [M$^+$]. Calculated for C$_{26}$H$_{18}$NiN$_4$, C 70.15, H 4.08, N 12.59; found C 69.99, H 3.99, N 12.56.

Images of the crystal structures have been produced using the software Mercury 2.3.[29-32] All cyclic voltammetry measurements were carried out in dry DCM using 0.3 M TBAPF$_6$ electrolyte in a three electrode system, with each solution being purged with N$_2$ prior to measurement. The working electrode was a 0.2 mm^2 Pt wire sealed in glass. The reference electrode was Ag/AgCl calibrated against Ferrocene/Ferrocenium in the background electrolyte, and the counter electrode was a Pt rod. All measurements were made at room temperature using an µAUTOLAB Type III potentiostat, driven by the electrochemical software GPES. Solution UV/Vis spectra were recorded in solution in DCM using a quartz cell of path length 1 cm on a Perkin-Elmer Lambda 9 spectrophotometer, controlled by a datalink PC, running UV/Winlab software and in thin films on a Jasco V-570 UV/Vis/NIR spectrophotometer. Magnetic susceptibility measurements were performed on powder samples from 1.8 to 300 K using a Quantum Design MPMS-XL SQUID magnetometer with MPMS MultiVu Application software to process the data. The magnetic field used was 0.1 T. Diamagnetic corrections were applied to the observed paramagnetic susceptibilities by using Pascal's constants. Single point and geometry optimisation calculations of the isolated complexes were carried out at the B3LYP/6-31G(d,p) level of theory[33-35], using Gaussian 03.[36] Time dependant DFT calculations were carried out using the polarisable continuum model (PCM) for DCM which takes into account the effect of solvation. The X-ray crystallographic coordinates were used as the starting structures. The molecular orbital isosurfaces were visualised using ArgusLab 4.0. Thin film XRD was carried out on a Rigaku ultraX-18HB at room temperature. Data were collected from 2θ angle of 5-40° at a rate of 2° per minute. Powder XRD was carried out using a Bruker AXS D8 diffractometer. All the substrates for deposition, except PET and the FETs, were cleaned in individual solutions of IPA, acetone and then chloroform prior to use. Deposition of

Ni(L1) was carried out via vacuum sublimation in a temperature range between 335°C and 345°C at a pressure of 5.0 x 10^{-4} Pa. This resulted in a growth rate of 0.2-0.4 Å/s which was monitored using a quartz crystal microbalance (QCM). Cu(L1) was deposited between 220°C and 240°C at a pressure of 7.5 x 10^{-4} Pa, which resulted in a growth rate of 0.2-0.4 Å/s. The less voltaile Co(L1) was deposited between 375°C and 385°C at a pressure of 5.2 x 10^{-4} Pa, which resulted in a growth rate of 0.1 Å/s. Ni(L2) was deposited between 425°C and 470°C at a pressure of 6.0 x 10^{-4} Pa, which resulted in a growth rate of 0.1 Å/s. The materials to be sublimed were heated inside an inert crucible by applying a current. Films of 50 nm thickness were produced according to the QCM. The actual thin film thickness was measured using a profileometer (Figure S2-S5). The FET substrates used have gold source and drain electrodes with a width of 2 μm and a gap of 2 or 8 μm. The measurements were carried out in darkness and under vacuum using a Keithley 2636A sourcemeter equipped with Labtracer 2.0 software. Imaging of thin films was carried out using a Hitachi S-4300 Scanning Electron Microscope.

Notes and references

[**Figure S15** Crystal structure of Co(L1)(Cl) in the presence of disordered toluene. **Table S4** Crystallographic information for Cu(L1), Ni(L2) and Co(L1)Cl.toluene. **Table S5** Selected bond lengths and angles of Cu(L1) and Ni(L2). **Figure S16** Profile of Ni(L1) showing a film thickness of approximately 100 nm. **Figure S17** Profile of Co(L1) showing a film thickness of approximately 90 nm. **Figure S18** Profile of Cu(L1) showing a film thickness of approximately 60 nm. **Figure S19** Profile of Ni(L2) showing a film thickness of approximately 90 nm. **Figure S20** Cyclic voltammagram of Co(L1) in 0.3M TBAPF$_6$/DCM at a scan rate of 0.1 V/s. **Figure S21** Differential pulse voltammogram of Co(L1) in 0.3M TBAPF$_6$/DCM scanning from 0 to 2 V. **Figure S22** Differential pulse voltammogram of Co(L1) in 0.3M TBAPF$_6$/DCM scanning from 0 to -2 V. **Figure S23** Cyclic voltammetry of Cu(L1) in 0.3M TBAPF$_6$/DCM.

Figure S24 Differential pulse voltammogram of Cu(L1) in 0.3M TBAPF$_6$/DCM. **Figure S25** Cyclic voltammetry of Ni(L1). **Figure S26** The Pt working electrode before (left) and after (right) scanning 5x between 2 and -2 V. **Figure S27** Cyclic voltammetry of Ni(L1). **Figure S28** Differential pulse voltammogram of of Ni(L1) in 0.3M TBAPF$_6$/DCM. **Figure S29** Cyclic voltammagram of Ni(L2) in 0.3M TBAPF$_6$/DCM at a scan rate of 0.1 V/s. **Figure S30** Differential pulse of Ni(L2) in 0.3M TBAPF$_6$/DCM. **Figure S31** χT vs. T plot of Co(L1) fit to the Curie Weiss law. **Figure S32** Comparison of structure obtained from geometry optimisation calculation versus the structure obtained from single crystal diffraction. **Table S6** Ni(L1) and Ni(L2) molecular orbitals generated from DFT calculations at the B3LYP/6-31G level of theory with the orbital energy in volts underneath. **Table S7** Co(L1) orbitals and energies from single point calculations at the B3LYP/6-31G(d,p) level of theory. **Figure S33** Orbital energies of the alpha and beta orbitals of Co(L1). Also displayed is the calculated spin density. **Table S8** Cu(L1) orbitals and energies from single point calculations at the B3LYP/6-31G(d,p) level of theory. **Figure S34** Comparison of structure obtained from geometry optimisation calculation versus the structure obtained from single crystal diffraction. **Table S9** Ni(L1) and Ni(L2) molecular orbitals generated from DFT calculations at the B3LYP/6-31G level of theory with the orbital energy in volts underneath. **Table S10** Co(L1) orbitals and energies from single point calculations at the B3LYP/6-31G(d,p) level of theory. **Figure S35** Orbital energies of the alpha and beta orbitals of Co(L1). Also displayed is the calculated spin density.

Table S11 Cu(L1) orbitals and energies from single point calculations at the B3LYP/6-31G(d,p) level of theory. **Figure S36** Cu(L1) calculation at the B3LYP/6-31G(d,p) level of theory showing the energies of the frontier orbitals and the spin density. **Figure S37** Cu(L1) calculation at the UB3LYP/TZVP level of theory showing the energies of the frontier orbitals and the spin density. **Figure S38** TD-DFT generated absorption spectra overlaid with an experimental solution measurement of Cu(L1).

Figure S39 TD-DFT generated absorption spectra overlaid with an experimental solution measurement of Co(L1). **Figure S40** TD-DFT generated absorption spectra overlaid with an experimental solution measurement of Ni(L2). **Table S12** TD-DFT assignment of electronic absorption spectra between 250 and 1000 nm. **Figure S41** Thin film diffraction pattern of Co(L1) in black, overlaid with the powder pattern in red. **Figure S42** Thin film diffraction pattern of Cu(L1) in black, overlaid with the powder pattern in red and single crystal generated pattern in blue.

Figure S43 Unit cell of Ni(L1) with the (200) plane highlighted in red. **Figure S44** Possible reflections from Ni(L2) thin film XRD. **Figure S45** Thin film absorption of Cu(L1) with solution spectrum overlaid. **Figure S46** Thin film absorption of Co(L1) with solution spectrum overlaid. **Figure S47** Thin film absorption of Ni(L1) with solution spectrum overlaid. **Figure S48** SEM image of Ni(L2). **Figure S49** Output characteristics of Ni(L1) on 2x2 μm substrates. **Figure S50** Transfer characteristics of Ni(L1) on 2x2 μm substrates. **Figure S51** Transfer characteristics of Cu(L1) on 2x2 μm substrates. **Figure S52** Magnetoresistance measurement on Cu(L1) at 4.35 K when applying a gate voltage of -60 V and a drain voltage of -40 V. **Figure S53** Output characteristics of Co(L1) on 2x2 μm substrates. **Figure S54** Transfer characteristics of Co(L1) on 2x2 μm substrates. **Figure S55** Output characteristics of Ni(L2) on 2x2 μm substrates. **Figure S56** Transfer characteristics of Ni(L2) on 2x2 μm substrates.]. See DOI: 10.1039/b000000x/

[1] Y. Zhang, X. Cai, Y. Bian and J. Jiang, Springer Berlin / Heidelberg, 2010, pp. 275-321.

[2] F. Garnier, X. Peng, G. Horowitz and D. Fichou, *Molecular Engineering*, 1991, **1**, 131-139.

[3] Z. Bao, A. J. Lovinger and A. Dodabalapur, *Applied Physics Letters*, 1996, **69**, 3066-3068.

[4] P. Ma, Y. Chen, X. Cai, H. Wang, Y. Zhang, Y. Gao and J. Jiang, *Synthetic Metals*, 2010, **160**, 510-515.

[5] D. Hohnholz, S. Steinbrecher and M. Hanack, *Journal of Molecular Structure*, 2000, **521**, 231-237.

[6] H.-S. Kim and C. C. Wamser, *Photochemical & Photobiological Sciences*, 2006, **5**, 955-960.

[7] M. V. Martinez-Diaz, G. de la Torre and T. Torres, *Chemical Communications*, 2010, **46**, 7090-7108.

[8] T. Minari, *Appl. Phys. Lett.*, 2007, **91**, 123501.

[9] M. H. Hoang, Y. Kim, S.-J. Kim, D. H. Choi and S. J. Lee, *Chemistry – A European Journal*, 2011, **17**, 7772-7776.

[10] N. B. Chaure and et al., *Science and Technology of Advanced Materials*, **12**, 025001.

[11] Liqiang Li, Qingxin Tang, Hongxiang Li, Wenping Hu, Xiaodi Yang, Zhigang Shuai, Yunqi Liu and D. Zhu, *Pure Appl. Chem.*, 2008, **80**, 2231–2240.

[12] V. Plyashkevich, T. Basova, I. Yushina and I. Igumenov, *Journal of Surface Investigation: X-ray, Synchrotron and Neutron Techniques*, 2008, **2**, 423-428.

[13] T. Basova, E. Kol'tsov, A. Hassan, A. Tsargorodskaya, A. Ray and I. Igumenov, *physica status solidi (b)*, 2005, **242**, 822-827.

[14] J. Puigdollers, C. Voz, M. Fonrodona, S. Cheylan, M. Stella, J. Andreu, M. Vetter and R. Alcubilla, *Journal of Non-Crystalline Solids*, 2006, **352**, 1778-1782.

[15] P. Mountford, *Chemical Society Reviews*, 1998, **27**, 105-116.

[16] L. G. Bell and J. C. Dabrowiak, *Journal of the Chemical Society, Chemical Communications*, 1975, 512-513.

[17] P. J. Lukes, J. A. Crayston, D. J. Ando, M. E. Harman and M. B. Hursthouse, *Journal of the Chemical Society, Perkin Transactions 2*, 1991, 1845-1849.

[18] L.-S. Lin, T. J. Marks, C. R. Kannewurf, J. W. Lyding, M. S. McClure, M. T. Ratajack and T.-C. Whang, *Journal of the Chemical Society, Chemical Communications*, 1980, 954-955.

[19] M. C. Weiss, G. Gordon and V. L. Goedken, *Inorganic Chemistry*, 1977, **16**, 305-310.

[20] P. J. Lukes, A. C. McGregor, T. Clifford and J. A. Crayston, *Inorganic Chemistry*, 1992, **31**, 4697-4699.

[21] P. J. Hochgesang and R. D. Bereman, *Inorganica Chimica Acta*, 1988, **149**, 69-76.

[22] C. Miry, D. Le Brun, J.-M. Kerbaol and M. L'Her, *Journal of Electroanalytical Chemistry*, 2000, **494**, 53-59.

[23] F. C. McElroy and J. C. Dabrowiak, *Journal of the American Chemical Society*, 1976, **98**, 7112-7113.

[24] W. E. Estes, D. P. Gavel, W. E. Hatfield and D. J. Hodgson, *Inorganic Chemistry*, 1978, **17**, 1415-1421.

[25] J. M. Assour and W. K. Kahn, *Journal of the American Chemical Society*, 1965, **87**, 207-212.

[26] L. G. Kaake, P. F. Barbara and X. Y. Zhu, *The Journal of Physical Chemistry Letters*, 2010, **1**, 628-635.

[27] M. Tello, M. Chiesa, C. M. Duffy and H. Sirringhaus, *Advanced Functional Materials*, 2008, **18**, 3907-3913.

[28] A. R. Cutler, C. S. Alleyne and D. Dolphin, *Inorganic Chemistry*, 1985, **24**, 2276-2281.

[29] R. Taylor and C. F. Macrae, *Acta Crystallographica Section B*, 2001, **57**, 815-827.

[30] I. J. Bruno, J. C. Cole, P. R. Edgington, M. Kessler, C. F. Macrae, P. McCabe, J. Pearson and R. Taylor, *Acta Crystallographica Section B*, 2002, **58**, 389-397.

[31] C. F. Macrae, I. J. Bruno, J. A. Chisholm, P. R. Edgington, P. McCabe, E. Pidcock, L. Rodriguez-Monge, R. Taylor, J. van de Streek and P. A. Wood, *Journal of Applied Crystallography*, 2008, **41**, 466-470.

[32] C. F. Macrae, P. R. Edgington, P. McCabe, E. Pidcock, G. P. Shields, R. Taylor, M. Towler and J. van de Streek, *Journal of Applied Crystallography*, 2006, **39**, 453-457.

[33] A. D. Becke, *J. Chem. Phys.*, 1993, **98**, 5648-5652.

[34] C. Lee, W. Yang and R. G. Parr, *Phys. Rev. B*, 1988, **37**, 785-789.

[35] R. Ditchfield, W. J. Hehre and J. A. Pople, *The Journal of Chemical Physics*, 1971, **54**, 724-728.

[36] M. J. Frisch, G. W. Trucks, H. B. Schlegel, G. E. Scuseria, M. A. Robb, J. R. Cheeseman, J. J. A. Montgomery, T. Vreven, K. N. Kudin, J. C. Burant, J. M. Millam, S. S. Iyengar, J. Tomasi, V. Barone, B. Mennucci, M. Cossi, G. Scalmani, N. Rega, G. A. Petersson, H. Nakatsuji, M. Hada, M. Ehara, K. Toyota, R. Fukuda, J. Hasegawa, M. Ishida, T. Nakajima, Y. Honda, O. Kitao, H. Nakai, M. Klene, X. Li, J. E. Knox, H. P. Hratchian, J. B. Cross, V. Bakken, C. Adamo, J. Jaramillo, R. Gomperts, R. E. Stratmann, O. Yazyev, A. J. Austin, R. Cammi, C. Pomelli, J. W. Ochterski, P. Y. Ayala, K. Morokuma, G. A. Voth, P. Salvador, J. J. Dannenberg, V. G. Zakrzewski, S. Dapprich, A. D. Daniels, M. C. Strain, O. Farkas, D. K. Malick, A. D. Rabuck, K. Raghavachari, J. B. Foresman, J. V. Ortiz, Q. Cui, A. G. Baboul, S. Clifford, J. Cioslowski, B. B. Stefanov, G. Liu, A. Liashenko, P. Piskorz, I. Komaromi, R. L. Martin, D. J. Fox, T. Keith, M. A. Al-Laham, C. Y. Peng, A. Nanayakkara, M. Challacombe, P. M. W. Gill, B. Johnson, W. Chen, M. W. Wong, C. Gonzalez and J. A. Pople, ed. Gaussian, Wallingford CT, 2004.